Chemical Engineering Journal 506 (2025) 160058

Contents lists available at ScienceDirect

Chemical Engineering Journal

journal homepage: www.elsevier.com/locate/cej

Local symmetry-breaking induces robust circularly polarized luminescence in achiral Dion-Jacobson tin-based perovskites

Jianwu Wei [a], Dongmei Wu [a], Liya Zhou [a], Peican Chen [a], Yibo Chen [b,*], Jie Tian [c], Jiahong Pan [c], Qi Pang [a,*], Jin Zhong Zhang [d]

[a] School of Chemistry and Chemical Engineering/State Key Laboratory of Featured Metal Materials and Life-cycle Safety for Composite Structures/Key Laboratory of Electrochemical Energy Materials//Guangxi Key Laboratory of Petrochemical Resource Processing and Process Intensification Technology, Guangxi University, Nanning 530004, Guangxi, PR China

[b] Institute of Clean Energy and Materials/Key Laboratory for Clean Energy and Materials, School of Chemistry and Chemical Engineering, Guangzhou University, Guangzhou, Guangdong 510006, PR China

[c] State Key Laboratory of Featured Metal Materials and Life-Cycle Safety for Composite Structures, School of Resources, Environment and Materials, Guangxi University, Nanning 530004, Guangxi, PR China

[d] Department of Chemistry and Biochemistry, University of California, Santa Cruz, CA 95064, United States

ARTICLE INFO

Keywords:
Circularly polarized luminescence
Achiral DJ tin-based perovskite
Chiral amplification
Asymmetric photopolymerization

ABSTRACT

The realization of circularly polarized luminescence (CPL) with high photoluminescence quantum yield (PLQY) and large luminescence dissymmetry g-factor ($|g_{lum}|$) in achiral lead-free perovskite poses a significant challenge. Herein, an achiral Dion-Jacobson (DJ) perovskite $HDASnBr_4$ (where HDA represents 1,6-diaminohexane) served as the main matrix to construct an R-DJ perovskite system (denoted as R-$HDASnBr_4$). This was achieved by incorporating a low dose of chiral ligand R-NEA ((R)-(+)-1-(1-naphthyl) ethylamine) to substitute for HAD locally. The R-$HDASnBr_4$ microcrystal exhibits warm white light CPL with both a large $|g_{lum}|$ of 0.022 and an impressive PLQY of 91 % at room temperature. Our investigation reveals that the rigid chiral ligand R-NEA partially replaces the flexible straight-chain HDA, inducing a local symmetry-breaking distortion of an inorganic framework in R-$HDASnBr_4$, which in turn stimulates robust CPL activity in R-$HDASnBr_4$. This strategy can also flexibly bind to other tin-based DJ perovskites, demonstrating its generality for chiral transfer. Additionally, we have demonstrated that R-$HDASnBr_4$ can facilitate controlled asymmetric photopolymerization under X-ray, offering potential utility in drug delivery and bioengineering applications.

1. Introduction

Circularly polarized luminescence (CPL) is attracting increasing interest due to its application potential in multiple fields, such as three-dimensional displays, spintronics, molecular probes, quantum computing, and optical information encryption [1]. Compared with the traditional physical approaches to obtaining CPL, CPL chemical materials offer significant advantages [2]. They can reduce energy loss, facilitate micro-device development, and enable precise control of chiral structures through molecular design for accurate CPL emission. Recently, chiral perovskites have become an ideal CPL material due to their easy preparation, low cost, and unique optical properties [3]. Notably, layered two-dimensional (2D) in particular can offer a facile and effective platform for synthesizing chiral materials due to the efficient chiral transfer in their soft lattice of high defect tolerance [4–6]. Many chiral 2D perovskites, formed by combining inorganic metal halide units with chiral cations, exhibit CPL properties with a relatively large luminescence dissymmetry g-factor ($|g_{lum}|$) [7,8]. However, overuse of chiral cations in chiral 2D perovskites leads to significant lattice distortion and consequently increase in nonradiative recombination while decreasing photoluminescence quantum yield (PLQY) [7,9]. Meanwhile, most chiral 2D perovskites are based on toxic lead substances, hampering their commercialization. The development of high-performance CPL-activated 2D lead-free perovskites with both high PLQY and large $|g_{lum}|$ remains a great challenge.

Achiral perovskites are widely used in photovoltaic and luminescent applications [10,11], with achiral 2D perovskites attracting more attention for their excellent stability and tunable optical and electrical

* Corresponding authors.
E-mail addresses: chenyibo@gzhu.edu.cn (Y. Chen), qipang@gxu.edu.cn (Q. Pang).

https://doi.org/10.1016/j.cej.2025.160058
Received 22 November 2024; Received in revised form 14 January 2025; Accepted 27 January 2025
Available online 28 January 2025

properties. For example, Xu *et al.* used benzyl carbamimidothioate hydrochloride to create efficient and stable 2D/3D perovskite solar cells [12]. In addition, achiral 2D perovskites consisting of achiral cations and inorganic octahedra also exhibit chirality-dependent soft lattices [13,14], making them ideal substitutes for the chiral ones [15,16]. For example, Pham *et al.* discovered CPL signals in achiral 2D perovskite $(BA)_2(MA)_{n-1}Pb_nI_{3n+1}$ (MA: Methylamine, BA: Butylamine) [15]. Meanwhile, Jana *et al.* discovered that the local symmetry breaking, rather than the global space group, of 2D perovskites is the key to chirality-dependent SOC [17]. Moreover, Haque *et al.* discovered that the local symmetry breaking induced in achiral 2D perovskites can achieve effective remote chirality transfer [18]. Inspired by these studies, identifying 2D lead-free perovskites with high PLQY and reasonably triggering local symmetry breaking of it to achieve strong CPL is desirable to simultaneously demonstrate high PLQY and large $|g_{lum}|$ values. However, such research has rarely been reported.

In this work, achiral 2D Dion-Jacobson (DJ) tin-based perovskite $HDASnBr_4$ microcrystal (where HDA refers to $(C_6H_{18}N_2)^{2+}$) was synthesized via acid precipitation, which shows intrinsic but low CPL activities. These materials are subsequently employed as the main substrate to prepare an excellent CPL active material (noted as R-$HDASnBr_4$) triggering by a small quantity of the chiral ligand R-NEA ((R)-(+)-1-(1-naphthyl) ethylamine) to replace the achiral organic cations (HDA). The theoretical calculations support that R-NEA induces the octahedral distortion of $HDASnBr_4$. And the as-prepared R-$HDASnBr_4$ showed a record high chiral activity of tin-based perovskites. This chirality amplification strategy can be extended to other tin-based DJ perovskites, demonstrating its generality for chiral transfer. Furthermore, R-$HDASnBr_4$ can be used to achieve X-ray-induced asymmetric photopolymerization at room temperature.

2. Results and discussion

Fig. 1a shows a schematic diagram for synthesizing R-NEA modified $HDASnBr_4$ microcrystal (Fig. S1), with the details described in the experimental section. The enantiomer S-NEA adopts the same strategy to modify $HDASnBr_4$. The R/S_x-$HDASnBr_4$ (x = 1, 2, or 3) samples were prepared by partially replacing HDA in $HDASnBr_4$ with R/S-NEA, where x refers to different amounts of R/S-NEA. Fig. 1b shows the XRD patterns of $HDASnBr_4$ and R_x-$HDASnBr_4$ (x = 1, 2, or 3) microcrystal powders, while Fig. S2 shows the XRD patterns of S_x-$HDASnBr_4$ (x = 1, 2, or 3). All samples have a clear periodic diffraction pattern (0 0 L) in the 2θ range of 5° – 25°. Meanwhile, $HDASnBr_4$ and R_x-$HDASnBr_4$ (x = 1, 2, or 3) films were obtained by the spin-coating method. XRD of all films showed the same periodic diffraction pattern (Fig. S3). This indicates that $HDASnBr_4$ and R_x-$HDASnBr_4$ have an ordered 2D structure, which is consistent with previous reports [19–21]. It also suggests that the incorporation of R-NEA does not destroy the initial 2D structure of $HDASnBr_4$. Fig. S4 shows that a slight shift is observed in the (0 0 2) plane of R_1-$HDASnBr_4$, R_2-$HDASnBr_4$, and R_3-$HDASnBr_4$ microcrystal powders at 7.82°, 7.83°, and 7.83° respectively, compared to 7.79° for $HDASnBr_4$. This can be ascribed to a slight lattice contraction caused by the partial replacement of HDA by R-NEA in the organic spacer layer. Moreover, Fig. S5 illustrates the energy-dispersive X-ray spectroscopy (EDS) mapping image of $HDASnBr_4$ and R_x-$HDASnBr_4$ microcrystal powders. The ratio of elements Sn and Br in $HDASnBr_4$, R_1-$HDASnBr_4$, R_2-$HDASnBr_4$, and R_3-$HDASnBr_4$ is about 1:4 (Table S1), which corresponds to the stoichiometric ratio (Sn: Br = 1:4) of 2D DJ $HDASnBr_4$. Moreover, as shown in Fig. S6, the addition of excess R-NEA results in new diffraction peaks appearing in the XRD spectrum of the resulting product that cannot be attributed solely to $HDASnBr_4$. This phenomenon can be attributed to the formation of metal halides $(R\text{-}NEA)_xSnBr_{x+2}$ [22–24]. Fig. 1c displays the liquid-state ^1H NMR spectra of $HDASnBr_4$ and R_x-$HDASnBr_4$ (x = 1, 2, or 3). The peaks at 1.50 ppm and 1.60 ppm belong to HDA and R-NEA, respectively. By integrating the peak area, the amount of R-NEA in R_1-$HDASnBr_4$, R_2-$HDASnBr_4$, and R_3-$HDASnBr_4$ microcrystal powders is calculated to be 1.8 %, 3.8 %, and 9.1 % respectively.

Fig. 2a shows the UV–visible absorption spectra of $HDASnBr_4$ and R_x-$HDASnBr_4$ (x = 1, 2, or 3). These samples show similar absorption edges

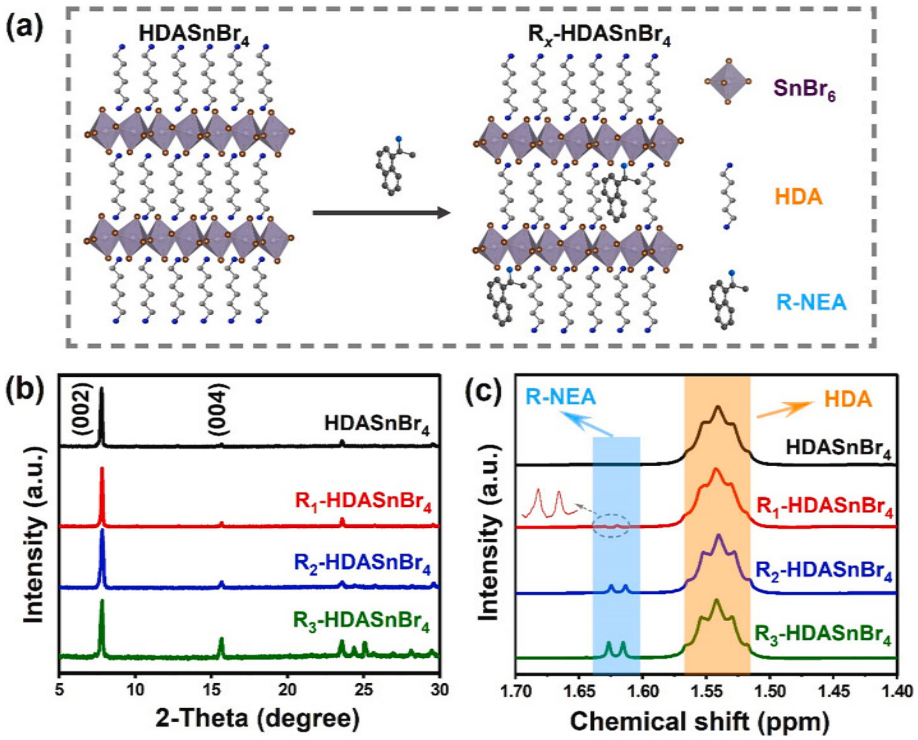

Fig. 1. (a) Schematic illustration of R-NEA modified $HDASnBr_4$ (R_x-$HDASnBr_4$ (x = 1, 2, or 3)), (b) XRD patterns, (c) ^1H NMR of $HDASnBr_4$ and R_x-$HDASnBr_4$ (x = 1, 2, or 3).

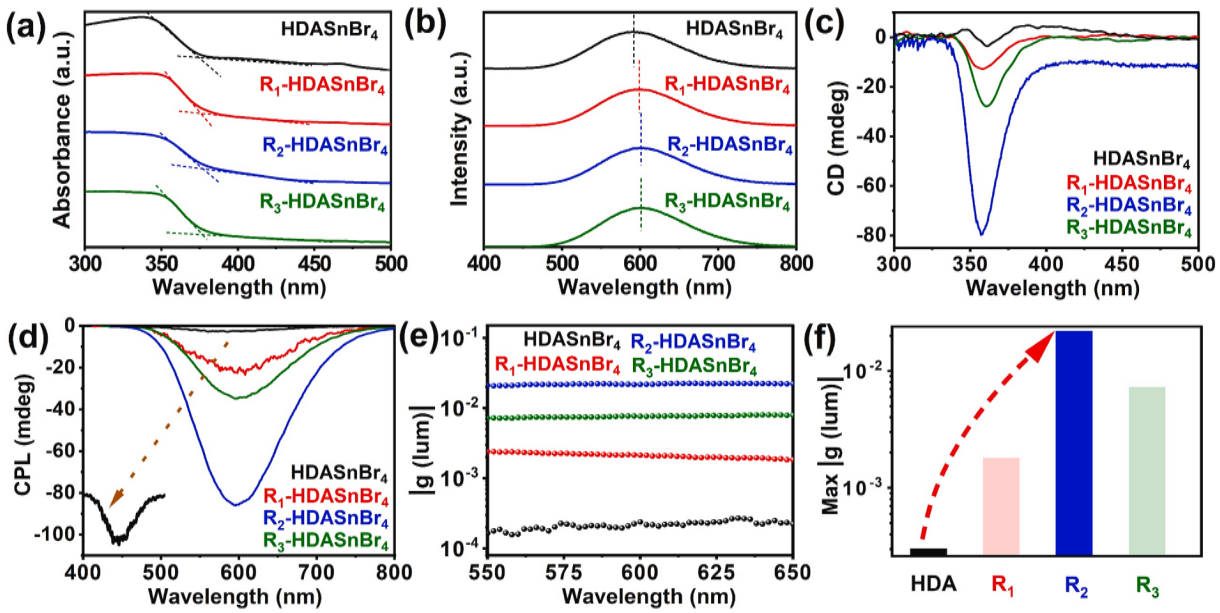

Fig. 2. (a) UV–visible absorption spectra, (b) PL spectra (λ_{ex} = 365 nm), (c) CD spectra, (d) CPL spectra (λ_{ex} = 365 nm), (e) $|g_{lum}|$ of $HDASnBr_4$ and R_x-$HDASnBr_4$ (x = 1, 2, or 3) at 550 – 650 nm, and (f) a comparison of the max $|g_{lum}|$ values for $HDASnBr_4$ and R_x-$HDASnBr_4$ (x = 1, 2, or 3). The label of HDA is for $HDASnBr_4$, and R_1, R_2, R_3 are for R_x-$HDASnBr_4$ (x = 1, 2, or 3).

at 374.5, 375.7, 376.5, and 376.8 nm, respectively. The photoluminescence excitation (PLE) peaks of $HDASnBr_4$, R_1-$HDASnBr_4$, R_2-$HDASnBr_4$, and R_3-$HDASnBr_4$ are located at 345.7, 346.4, 351.2, and 351.5 nm, respectively (Fig. S7). These samples exhibit a broadband photoluminescence (PL) centered at 592.4, 599.3, 601.1, and 601.5 nm, respectively, upon the excitation at 365 nm (Fig. 2b). According to the PLE and PL spectra, the Stoke shift of $HDASnBr_4$, R_1-$HDASnBr_4$, R_2-$HDASnBr_4$, and R_3-$HDASnBr_4$ are calculated to be 1.49, 1.51, 1.47, and 1.47 eV respectively. In addition, Fig. S8 shows the time-resolved PL (TRPL) decay profiles of $HDASnBr_4$ and R_x-$HDASnBr_4$ (x = 1, 2, or 3), which can be fitted using a double exponential function (Equation S1). The PL lifetime (τ_{obs}) values of $HDASnBr_4$, R_1-$HDASnBr_4$, R_2-$HDASnBr_4$, and R_3-$HDASnBr_4$ are 6.24, 5.73, 5.44, and 5.28 μs, respectively. All samples show large Stoke shifts and long τ_{obs}, consistent with the Self-trapped excitons (STEs) emission characteristics of the reported DJ tin-based perovskites [19,25]. Meanwhile, S_x-$HDASnBr_4$ (x = 1, 2, or 3) also exhibits similar STE emission characteristics (Supplementary Note 1, Fig. S9). Moreover, slight redshifts are observed in the absorption edges, PLE spectra, and PL spectra of R/S_x-$HDASnBr_4$ (x = 1, 2, or 3) compared to those of $HDASnBr_4$. This may be due to the addition of R/S-NEA that increases the lattice distortion of $HDASnBr_4$ and results in a decrease in the STE excited state energy [26–28].

The PLQY of $HDASnBr_4$, R_1-$HDASnBr_4$, R_2-$HDASnBr_4$, and R_3-$HDASnBr_4$ are 93 %, 92 %, 91 %, and 88 %, respectively (Fig. S10). Meanwhile, the PLQY of S_1-$HDASnBr_4$, S_2-$HDASnBr_4$, and S_3-$HDASnBr_4$ are 91 %, 90 %, and 88 %, respectively (Fig. S11). The high PLQY of all samples is attributed to high crystal quality [19,20,22], which has been well maintained after the modification of a small amount of R/S-NEA. By combining PLQY and τ_{obs}, the radiation recombination rate (k_r) and non-radiation recombination rate (k_{nr}) can be calculated using Equations S2 and S3 [29], and the results are collected in Table S2 in Supporting Information. The k_{nr} values of $HDASnBr_4$, R_1-$HDASnBr_4$, R_2-$HDASnBr_4$, and R_3-$HDASnBr_4$ are 0.011, 0.014, 0.017, and 0.023 μs^{-1}, respectively. Compared to $HDASnBr_4$, the PLQY of R_1-$HDASnBr_4$, R_2-$HDASnBr_4$, and R_3-$HDASnBr_4$ decrease, while their k_{nr} increase. This could be due to the monovalent R-NEA replacing divalent HDA, creating additional cation vacancy defects that facilitate non-radiative recombination.

Fig. 2c shows the CD spectra of $HDASnBr_4$ and R_x-$HDASnBr_4$ (x = 1, 2, or 3). We fabricated transparent thin films for CD testing via the KBr die-casting method, with the details described in the Supporting Information. The influence of linear birefringence and linear circular dichroism (LBLD) on CD signal was eliminated by flipping the film for CD test, and the CD signal of the sample was obtained by Equation S4 in Supporting Information [30]. In the range of 340–370 nm which corresponds to the absorption band in the UV spectrum, $HDASnBr_4$ shows a CD signal with a maximum value of −3.5 mdeg. The CD signal observed in $HDASnBr_4$ without chiral material is attributed to octahedral distortion caused by Sn^{2+} with a lone pair of electrons and octahedral tilting caused by HAD [16,32,33]. Upon triggering with R-NEA, R_1-$HDASnBr_4$, R_2-$HDASnBr_4$, and R_3-$HDASnBr_4$ show an intensified CD signal with a maximum value of −12.7, −79.8, and −27.8 mdeg, respectively.

We used the same thin film for CD testing in the CPL testing. Fig. 2d shows the CPL spectra of $HDASnBr_4$ and R_x-$HDASnBr_4$ (x = 1, 2, or 3), which align well with the PL peaks observed in the PL spectra. $HDASnBr_4$, R_1-$HDASnBr_4$, R_2-$HDASnBr_4$, and R_3-$HDASnBr_4$ show CPL signals with a maximum value of −2.66, −22.1, −85.8, and −34.6 mdeg in the range of 550 – 650 nm, respectively. This result indicates a significantly enhanced CPL signal after $HDASnBr_4$ is modified by R-NEA. In addition, the corresponding $|g_{lum}|$ values in the range of 550 – 650 nm are shown in Fig. 2e. The maximum $|g_{lum}|$ values for R_1-$HDASnBr_4$, R_2-$HDASnBr_4$, and R_3-$HDASnBr_4$ are 1.8×10^{-3}, 2.2×10^{-2}, and 7.6×10^{-3}, respectively, which are significantly higher than that of 2.3×10^{-4} for $HDASnBr_4$ (Fig. 2f). The comprehensive chiral optical property of R_2-$HDASnBr_4$ has been the most outstanding compared to that of the 2D perovskite reported in previous works (Table S3).

Meanwhile, we explored the chirality of S_x-$HDASnBr_4$ (x = 1, 2, or 3). Fig. S12 shows the CD and CPL spectra of S_x-$HDASnBr_4$. Notably, S_2-$HDASnBr_4$ exhibits the strongest CPL signal, accompanied by a maximum $|g_{lum}|$ of 1.1×10^{-2}. Compared with the CD and CPL signal of R-$HDASnBr_4$, that of S-$HDASnBr_4$ show reversed signs due to the mirror symmetry of R-NEA and S-RNEA. The above results demonstrate that even a small amount of chiral R/S-NEA to achiral $HDASnBr_4$ can yield R_2/S_2-$HDASnBr_4$ with significantly enhanced CPL activity.

Based on the CD and CPL results, The content of the R-NEA is not positively correlated with the chiral activity it triggers in perovskites. Although it might be expected that higher concentrations of chiral R-NEA would lead to more efficient chiral transfer in R_3-$HDASnBr_4$ as compared to R_2-$HDASnBr_4$, the experimental results reveal the opposite,

consistent with the previously reported results [33,34]. The calculated PLQY and k_{nr} values indicate that an increased concentration of chiral R-NEA leads to an excess of organic cation defect vacancies in R_3-$HDASnBr_4$. We believe that the excessive R-NRA and the defects it causes lead to the disordered lattice distortion in R_3-$HDASnBr_4$, which hinders chiral transfer [35]. Meanwhile, it weakens the hydrogen bonding effect, reducing the chiral transfer efficiency [36]. As a result, the CD and CPL intensity is weakened. Furthermore, it intensifies the non-radiative recombination route as well as gives rise to CPL scattering [37,38]. However, in general, the modification of R-NEA at various concentrations resulted in enhanced CPL activity of $HDASnBr_4$.

We further explored the effect of R/S-NEA content on chiral activity in another DJ tin-based perovskite $ODASnBr_4$ (ODA stands for 1,8-Octyldiamine), which differs in the carbon chain length (C_x) of the spacer cations from $HDASnBr_4$ (Fig. S13). The amount of R-NEA in R_1-$ODASnBr_4$, R_2-$ODASnBr_4$, and R_3-$ODASnBr_4$ is calculated to be 2.3 %, 4.2 %, and 10.9 % respectively (Fig. S14). The CPL and DC values for R_1-$ODASnBr_4$, R_2-$ODASnBr_4$, and R_3-$ODASnBr_4$ were measured in Fig. S15a. The maximum $|g_{lum}|$ of R_1-$ODASnBr_4$, R_2-$ODASnBr_4$, and R_3-$ODASnBr_4$ is 2.9×10^{-3}, 6.1×10^{-3}, and 4.2×10^{-3}, respectively (Fig. S15b). Meanwhile, Fig. S16a shows that the S_x-$ODASnBr_4$ ($x = 1$, 2, or 3) presents a CPL signal that mirrors that of the R_x-$ODASnBr_4$ ($x = 1$, 2, or 3). The maximum $|g_{lum}|$ of S_1-$ODASnBr_4$, S_2-$ODASnBr_4$, and S_3-$ODASnBr_4$ is 2.8×10^{-3}, 5.3×10^{-3}, and 4.4×10^{-3}, respectively (Fig. S16b). The chiral cation substitution strategy also achieves strong CPL activity in R/S_x-$ODASnBr_4$ ($x = 1$, 2, or 3), indicating the generality of this strategy.

Additionally, R_x-$ODASnBr_4$ (x = 1, 2, or 3) exhibits lower $|g_{lum}|$ values than R_x-$HDASnBr_4$ (x = 1, 2, or 3). Subtle differences in C_x between R_x-$ODASnBr_4$ (C_8) and R_x-$HDASnBr_4$ (C_6) lead to large differences in $|g_{lum}|$ values, prompting a search for the underlying mechanisms. Density Functional Theory (DFT) calculations were used to investigate how the C_x difference between $ODASnBr_4$ and $HDASnBr_4$ affects the chiral activity. This was achieved by theoretically integrating an equal quantity of R-NAE into both materials via theoretical modeling, named R-$ODASnBr_4$ and R-$HDASnBr_4$, respectively. A detailed description of the calculation method is given in Supporting Information.

Fig. 3a and b illustrate the process of introducing equal amounts of R-NEA into $HDASnBr_4$ and $ODASnBr_4$ and the corresponding $[SnBr_6]^{4-}$octahedra. The octahedral distortion is characterized by the bond length distortion index Δ_d and bond angle variance (σ^2), which are obtained via Equations S5 and S6 in Supporting Information [30,39]. Fig. 3c shows Δ_d values of 1.28×10^{-4}, 74.09×10^{-4}, 0.75×10^{-4} and 60.48×10^{-4} for $HDASnBr_4$, R-$HDASnBr_4$, $ODASnBr_4$ and R-$ODASnBr_4$, respectively. The σ^2 values of $HDASnBr_4$, R-$HDASnBr_4$, $ODASnBr_4$ and R-$ODASnBr_4$ were 9.61, 96.71, 3.70 and 87.4 deg^2, respectively, as shown in Fig. 3d. Before introducing, the octahedral distortion of $HDASnBr_4$ and $ODASnBr_4$ originates from the lone pair of electrons of $Sn^{2+}$and the octahedral tilting induced by HDA and ODA [15,31,32]. Meanwhile, the octahedral distortion in $HDASnBr_4$ is larger than that in $ODASnBr_4$. This is due to the closer proximity of the inorganic octahedral layers in $HDASnBr_4$, leading to stronger interlayer coupling [40,41], which triggers larger octahedral distortion. Upon introduction with R-NEA, compared to R-$ODASnBr_4$, the interlayer space in R-$HDASnBr_4$ is tighter to accommodate the more significant lattice distortion resulting from the intervention of a rigid R-NEA [42,43]. Meanwhile, significant interlayer interactions are possible in R-$HDASnBr_4$ due to the stronger interlayer coupling [13]. It is conducive to the remote chirality transfer within the lattice.

Further, with R_2-$HDASnBr_4$ as the target, an in-depth exploration of the mechanisms of strong chirality will be carried out. We measured the temperature-dependent PL spectra (Fig. S17) to evaluate the degree of

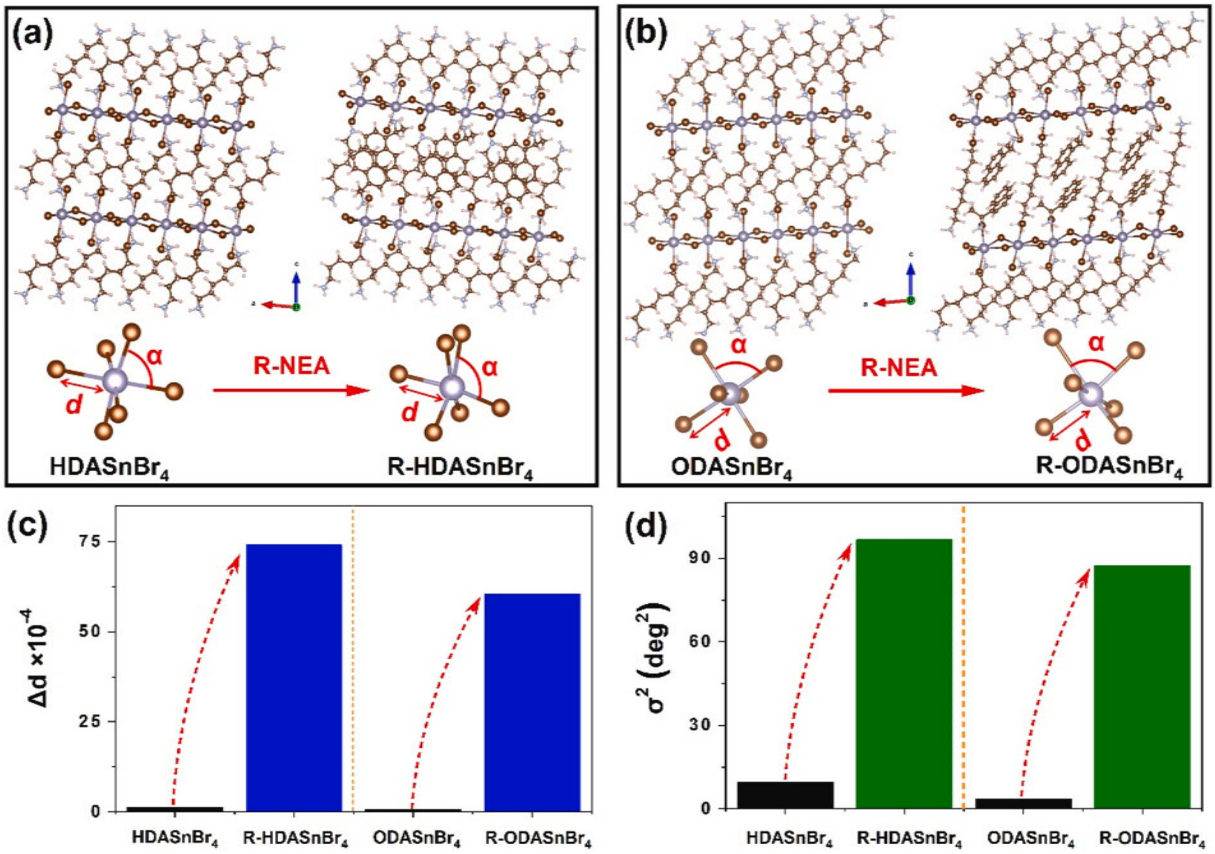

Fig. 3. $[SnBr_6]^{4-}$ octahedron of (a) $HDASnBr_4$ and R-$HDASnBr_4$, (b) $ODASnBr_4$, and R-$ODASnBr_4$, (c) Δd and (d) σ^2 of $HDASnBr_4$, R-$HDASnBr_4$, $ODASnBr_4$, and R-$ODASnBr_4$.

lattice distortion of $HDASnBr_4$ and R_x-$HDASnBr_4$ ($x = 1$, 2, or 3). Huang-Rhys factor (S), defined as an indicator of the exciton-phonon coupling, was calculated via Equation S7 in Supporting Information.[44,45] The S value of R_2-$HDASnBr_4$ is 22.2, higher than the 15.5 for $HDASnBr_4$. The increased S value of R_2-$HDASnBr_4$ indicates a stronger exciton-phonon coupling, associated with intensified transient elastic lattice distortion, which corresponds to enhanced octahedral distortion according to the previous reports [46–49].

Moreover, Fig. S18a shows the high-resolution XPS spectra of Br 3d in $HDASnBr_4$ and R_2-$HDASnBr_4$. The peaks at 67.99 and 69.11 eV correspond to the $3d_{5/2}$ and $3d_{3/2}$ energy levels of $HDASnBr_4$, while the Br 3d peaks of R_2-$HDASnBr_4$ shift towards higher binding energies compared to that of $HDASnBr_4$, at 68.90 and 69.99 eV. The alteration in electronic structures of Br is ascribed to asymmetric hydrogen bonding between R-NEA and Br that results in a change in the chemical environment around the $[SnBr_6]^{4-}$ octahedron [34,50]. Fig. S18b shows the liquid-state ^{13}C NMR spectrum of the R-NEA and R_2-$HDASnBr_4$. The distinctive peak of the C adjacent to the amino group in R-NEA is at 46.00 ppm, while that of the R_2-$HDASnBr_4$ is at 46.19 ppm. The increased chemical shift of the C peak in the R_2-$HDASnBr_4$ further confirms the formation of asymmetric hydrogen bonds between the amino group of R-NEA and Br^- [51], consistent with the results of the XPS spectrum.

Furthermore, Fig. S19 shows the CPL, DC value, and g_{lum} of (R)-(+)-1-phenylethylamine modified $HDASnBr_4$ and D(+)-phenylalaninol modified $HDASnBr_4$ in their respective optimal doping amounts. A $|g_{lum}|$ of 2.8×10^{-3} and 2.3×10^{-3} were measure for (R)-(+)-1-phenylethylamine modified $HDASnBr_4$ and D(+)-phenylalaninol modified $HDASnBr_4$, respectively. The findings indicate that this strategy applies to various chiral molecules. We contend that the asymmetric hydrogen bonding between the chiral molecule and $HDASnBr_4$ causes local lattice distortion, which induces symmetry-breaking of the inorganic framework [15,52]. This local symmetry-breaking achieves the overall chiral-related distortion through effective remote transmission [17,53], which is the origin of the CPL effect (Supplementary Note 2, Fig. S20). In this regard, combining achiral DJ structures with diverse chiral molecules presents extensive opportunities for creating high-performance CPL active materials.

Fig. S21 illustrates the XRD patterns and PL spectra of R_2-$HDASnBr_4$ microcrystal powders that were stored in an environment with an average temperature of 25 °C and an average humidity of 30 % over 30 days. It exhibits a distinct periodic diffraction pattern (0 0 L) within the 2θ range of 5° to 25° in XRD patterns, which suggests the structural stability of the material. Furthermore, the sample retains approximately 89.0 % of its original PL intensity, indicating its excellent optical stability. Fig. 4a-c shows the CPL and DC value of R_2-$HDASnBr_4$ in different

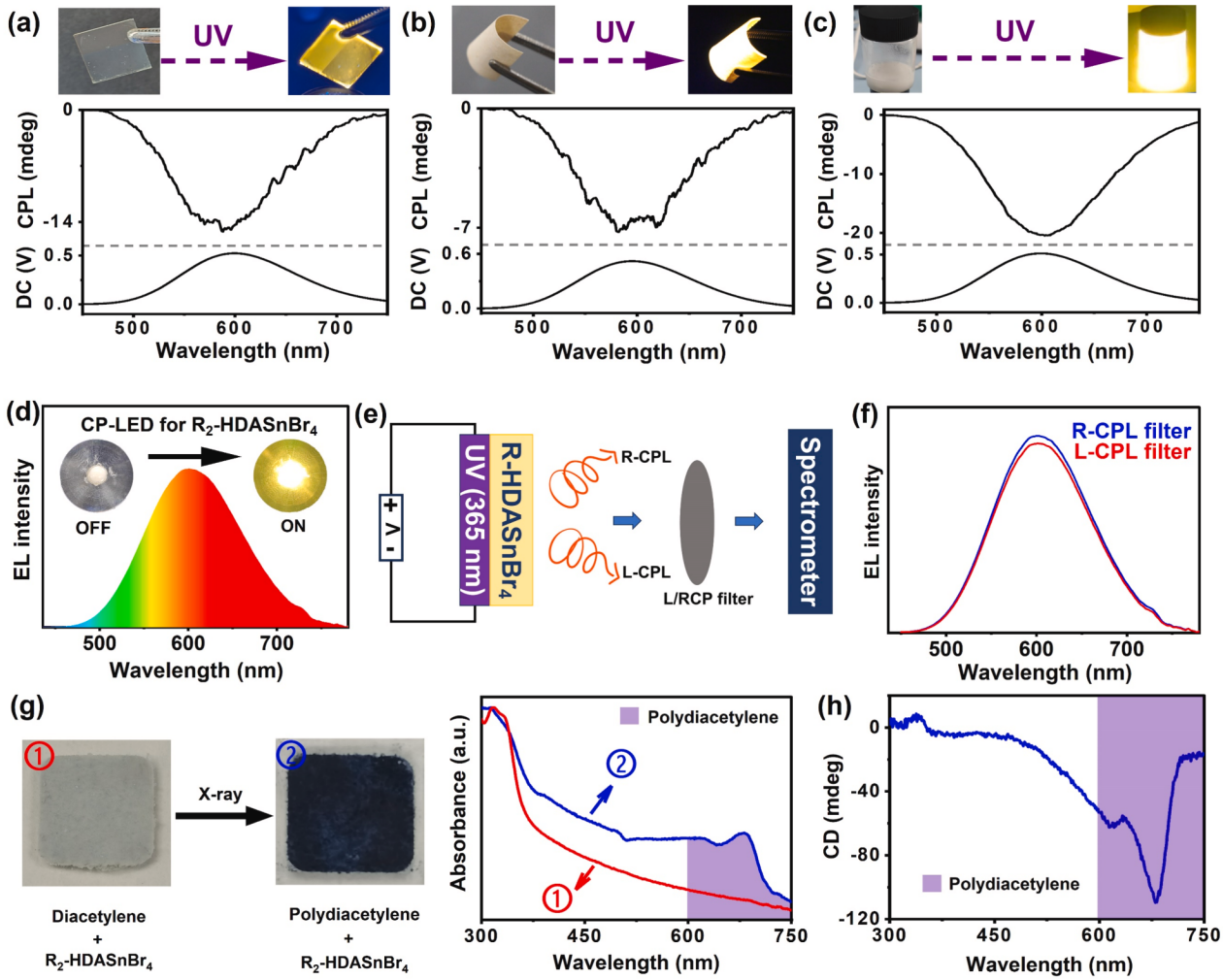

Fig. 4. CPL spectra ($\lambda_{ex} = 365$ nm) and DC of R_2-$HDASnBr_4$ in (a) thin film, (b) flexible film, and (c) colloidal solutions. (d) EL spectrum and lighting image of a UV (365 nm)-pumped CP-LED prototype based on R_2-$HDASnBr_4$. (e) Schematic diagram of CPL detection for the UV-pumped CP-LED. (f) CPL spectra produced by CP-LED after passing through the LCP and RCP filters. (g) Transformation of R_2-$HDASnBr_4$/diacetylene composite film into R_2-$HDASnBr_4$/polydiacetylene composite film under X-ray irradiation and the UV–vis absorption spectra of R_2-$HDASnBr_4$/diacetylene and R_2-$HDASnBr_4$/polydiacetylene composite films. (h) CD spectra of R_2-$HDASnBr_4$/polydiacetylene composite film. Inset: (a) photos of the deactivation and activation of the device.

states of thin film, flexible film, and colloidal solutions. All of them show the same profile as the R_2-$HDASnBr_4$ microcrystal, indicating their consistent CPL activity across different media and suitability for various applications. Meanwhile, owing to the difference in the effective content and light transmittance of R_2-$HDASnBr_4$ in different forms, there are intrinsic differences in the CPL strengths exhibited by thin films, flexible films, and colloidal solutions.

Fig. 4d displays the electroluminescence (EL) spectrum of the UV-pumped circularly polarized (CP)-LED. The CPL performance of UV-pumped CP-LED was evaluated, and the principle behind this process is illustrated in Fig. 4e. Fig. 4f shows that the UV-pumped CP-LED achieved CPL directly without an optical polarizer [54]. The circular polarization characteristics of the prepared CP-LED are consistent with the chirality of R_2-$HDASnBr_4$, thereby demonstrating its feasibility and potential for the preparation of CP-LED.

We also explored the potential of R_2-$HDASnBr_4$ for *in-situ* asymmetric photochemistry. Fig. 4g depicts a white hybrid film composed of diacetylene monomer/R_2-$HDASnBr_4$, which transitions to a blue color upon X-ray exposure. The UV–visible absorption of the blue hybrid film shows extra absorption bands in the range of 600 – 750 nm compared with that of the white hybrid film, which indicates that the polydiacetylene was successfully synthesized [55]. The CD spectrum of polydiacetylene/R_2-$HDASnBr_4$ hybrid films is shown in Fig. 4h. The influence of LBLD on CD signal was eliminated by flipping the film for CD test. A clear CD signal in the range of 600–750 nm corresponding to the absorption band of the polydiacetylene was observed, indicating the chirality of the prepared polydiacetylene. We contend that R_2-$HDASnBr_4$ functions as a chiral inducer and CPL source in this *in situ* asymmetric photochemistry [55,56].

Meanwhile, we used the mirror enantiomer S_2-$HDASnBr_4$ for achieving *in-situ* asymmetric photopolymerization of achiral diacetylene monomers under room temperature X-ray irradiation. As shown in Fig. S22, the CD signal of polydiacetylene/S_2-$HDASnBr_4$ mixtures is similarly mirror-image enantiomorphic to that of the polydiacetylene/R_2-$HDASnBr_4$ mixtures. The phenomenon can be attributed to that R_2-$HDASnBr_4$ and S_2-$HDASnBr_4$ are mirror enantiomers, causing mirror-symmetric changes in the molecular conformation and electronic structure of polydiacetylene. Consequently, this leads to mirror-image absorption of left- and right-handed CPL. This means that the chirality of the resulting polydiacetylene is affected by the chiral optical activity of the R_2/S_2-$HDASnBr_4$, suggesting that CD signals are induced by the R_2/S_2-$HDASnBr_4$ rather than intrinsic to the polydiacetylene itself.

Furthermore, the CD spectra of R-NEA/Polydiacetylene hybridized films and $HDASnBr_4$/Polydiacetylene hybridized films under X-ray irradiation do not exhibit the characteristic CD peak of polydiacetylene (Fig. S23). This is due to that neither R-NEA nor $HDASnBr_4$ alone can provide effective chiral induction and CPL to achieve helical polymerization of polydiacetylene. This indicates that the chiral activity of polydiacetylene is induced by the R_2-$HDASnBr_4$ under X-ray irradiation, rather than R-NEA or $HDASnBr_4$, which reveals the potential of R_2-$HDASnBr_4$ to assist X-ray-induced asymmetric photopolymerization at room temperature.

3. Conclusion

In summary, the incorporation of a low dose (3.8 %) of chiral ligand R-NEA into $HDASnBr_4$ via acid precipitation successfully yielded R-$HDASnBr_4$. The resultant R-$HDASnBr_4$ demonstrates robust CPL characteristics, with a significant $|g_{lum}|$ value of 0.022 and a high PLQY of 91 %. Theoretical calculations indicate that substituting flexible straight-chain HDA with rigid chiral R-NEA, which is characterized by larger spatial volume substitutions, induces chirality-related octahedral distortion in R-$HDASnBr_4$. This distortion is enhanced by efficient interlayer transfer, facilitating remote chirality transfer. Consequently, this leads to high CPL performance in R-$HDASnBr_4$. Moreover, R-$HDASnBr_4$ is employed to facilitate asymmetric synthesis under X-ray, offering potential applications in drug delivery and bioengineering applications. This study showcases a simple yet effective strategy to obtain DJ tin (II) based perovskites with high CPL by using a small amount of chiral organic compounds and robust interlayer interactions.

4. Experimental

4.1. Materials

1,6-hexanediamine (HDA, 99.0 %), 1,8-Octanediamine (ODA, 99.0 %), stannous oxide (SnO, 98.0 %), hydrogen bromide (HBr, 48 wt% in H_2O), (R/S–) −(+)-1-(1-naphthyl) ethylamine (R/S-NEA, 98.0 %), hexane (Hex, 99.0 %), hypophosphorous acid (H_3PO_2, 50 wt% solution in water) were purchased from Adamas. Cellulose Nanocrystals (CNCs, Cellulose Lab, Canada). All were used directly without further purification.

4.2. Preparation of RNEA-modified $HDASnBr_4$

1,6-hexanediamine (0.200 mmol), SnO (0.200 mmol), H_3PO_2 (15 mL), and HBr (5.0 mL) were placed into a 50.0 ml two-neck flask and stirred under vacuum at 373.0 K for 30 min. Then, nitrogen was introduced, the temperature was lowered to 353.0 K, the solution was concentrated to 10 mL by vacuum distillation, and then R-NEA was introduced into the reaction with HDA at molar ratios of 0.3:1, 0.6:1, and 0.9:1, resulting in corresponding products denoted as R_1-$HDASnBr_4$, R_2-$HDASnBr_4$, and R_3-$HDASnBr_4$ respectively. The crude product solution was kept in an ice bath for 24 h until the $HDASnBr_4$ crystals precipitously formed. The solid–liquid mixture was separated by negative pressure filtration, and the solid was placed in a vacuum-drying oven of 333 K for two hours after washing with n-hexane.

CRediT authorship contribution statement

Jianwu Wei: Writing – original draft, Investigation, Formal analysis, Data curation, Conceptualization. **Dongmei Wu:** Data curation. **Liya Zhou:** Writing – review & editing. **Peican Chen:** Conceptualization. **Yibo Chen:** Conceptualization. **Jie Tian:** Conceptualization. **Jiahong Pan:** Conceptualization. **Qi Pang:** Writing – review & editing. **Jin Zhong Zhang:** Writing – review & editing.

Declaration of competing interest

The authors declare that they have no known competing financial interests or personal relationships that could have appeared to influence the work reported in this paper.

Acknowledgments

This work was supported by the National Natural Science Foundation of China (Grant No. 22365005), the Central Guidance on the Local Science and Technology Development Fund of Guangxi Province (Gui Ke ZY23055001), Guangxi Natural Science Foundation (2024GXNSFDA010050), Innovation Project of Guangxi Graduate Education (Grant No. A3040022006), BRICS STI Framework Programme (No. 52261145703), JZZ is grateful to the US NSF for financial support (CHE-2203633).

Appendix A. Supplementary data

Supplementary data to this article can be found online at https://doi.org/10.1016/j.cej.2025.160058.

Data availability

Data will be made available on request.

References

[1] W.R. Kitzmann, J. Freudenthal, A.-P.-M. Reponen, et al., Fundamentals, advances, and artifacts in circularly polarized luminescence (CPL) spectroscopy, *Adv. Mater.* 35 (44) (2023) 2302279.

[2] R. Zhang, H. Zhong, K. Yang, et al., Energy transfer for constructing circularly polarized luminescence materials: recent progress and future prospects, *Adv. Funct. Mater.* (2024) 2417308.

[3] G. Long, R. Sabatini, M.I. Saidaminov, et al., Chiral-perovskite optoelectronics, *Nat. Rev. Mater.* 5 (6) (2020) 423–439.

[4] J.-H. Yang, Q. Yuan, B.I. Yakobson, Chemical trends of electronic properties of two-dimensional halide perovskites and their potential applications for electronics and optoelectronics, *J. Phys. Chem. C* 120 (43) (2016) 24682–24687.

[5] H.P. Lu, C.X. Xiao, R.Y. Song, et al., Highly Distorted chiral two-dimensional tin iodide perovskites for spin polarized charge transport, *J. Am. Chem. Soc.* 142 (30) (2020) 13030–13040.

[6] C. Coccia, M. Morana, A. Mahata, et al., Ligand-induced chirality in $ClMBA_2SnI_4$ 2D perovskite**, *Angew. Chem. Int. Ed.* 63 (10) (2024) e202318557.

[7] S.P. Liu, M. Kepenekian, S. Bodnar, et al., Bright circularly polarized photoluminescence in chiral layered hybrid lead-halide perovskites, *Sci. Adv.* 9 (35) (2023) eadh5083.

[8] C.H. Yang, S.B. Xiao, H. Xiao, et al., Efficient red-emissive circularly polarized electroluminescence enabled by Quasi-2D perovskite with chiral spacer cation, *ACS Nano* 17 (8) (2023) 7830–7836.

[9] G. Long, C. Jiang, R. Sabatini, et al., Spin control in reduced-dimensional chiral perovskites, *Nat. Photonics* 12 (9) (2018) 528–533.

[10] H. Yang, Z. Xu, H. Wang, et al., Iodide management and oriented crystallization modulation for high-performance all-air processed perovskite solar cells, *Adv. Mater.* 36 (49) (2024) 2411721.

[11] C. Gong, H. Li, H. Wang, et al., Silver coordination-induced N-doping of PCBM for stable and efficient inverted perovskite solar cells, *Nat. Commun.* 15 (1) (2024) 4922.

[12] Z. Xu, Z. Guo, H. Li, et al., Efficient and stable inverted MA/Br-free 2D/3D perovskite solar cells enabled by α-to-δ phase transition inhibition and crystallization modulation, Energy Environ. Sci. 18 (2025) 1354–1365.

[13] M. Pazoki, R. Imani, A. Röckert, et al., Electronic structure of 2D hybrid perovskites: rashba spin-orbit coupling and impact of interlayer spacing, *J. Mater. Chem. A* 10 (39) (2022) 20896–20904.

[14] M.K. Jana, R.Y. Song, H.L. Liu, et al., Organic-to-inorganic structural chirality transfer in a 2D hybrid perovskite and impact on Rashba-Dresselhaus spin-orbit coupling, *Nat. Commun.* 11 (1) (2020) 4699.

[15] M.T. Pham, E. Amerling, T.A. Ngo, et al., Strong Rashba-Dresselhaus effect in nonchiral 2D Ruddlesden-popper perovskites, *Adv. Opt. Mater.* 10 (1) (2021) 2101232.

[16] G.X. Zhan, J.R. Zhang, L.H. Zhang, et al., Stimulating and manipulating robust circularly polarized photoluminescence in achiral hybrid perovskites, *Nano Lett.* 22 (10) (2022) 3961–3968.

[17] M.K. Jana, R.Y. Song, Y. Xie, et al., Structural descriptor for enhanced spin-splitting in 2D hybrid perovskites, *Nat. Commun.* 12 (1) (2021) 4982.

[18] M.A. Haque, A. Grieder, S.P. Harvey, et al., Remote chirality transfer in low-dimensional hybrid metal halide semiconductors, Nat. Chem.17 (2025) 29–37.

[19] A. Mandal, S. Roy, A. Mondal, et al., Spacer switched two-dimensional tin bromide perovskites leading to ambient-stable near-unity photoluminescence quantum yield, *J. Phys. Chem. Lett.* 13 (39) (2022) 9103–9113.

[20] C.R. Kagan, D.B. Mitzi, C.D. Dimitrakopoulos, Organic-inorganic hybrid materials as semiconducting channels in thin-film field-effect transistors, *Science* 286 (5441) (1999) 945–947.

[21] A. Mandal, S.K. Khuntia, D. Mondal, et al., Spin texture sensitive photodetection by Dion–Jacobson tin halide perovskites, *J. Am. Chem. Soc.* 145 (45) (2023) 24990–25002.

[22] A. Ishii, T. Miyasaka, Direct detection of circular polarized light in helical 1d perovskite-based photodiode, *Sci. Adv.* 6 (46) (2020) eabd3274.

[23] J.T. DuBose, A. Christy, J. Chakkamalayath, et al., Trap or triplet? Excited–state interactions in 2D perovskite colloids with chromophoric cations, *ACS Nano* 17 (19) (2023) 19052–19062.

[24] S. Shrestha, M.X. Li, S. Park, et al., Room temperature valley polarization via spin selective charge transfer, *Nat. Commun.* 14 (1) (2023) 5234.

[25] S. Wang, J. Popović, S. Burazer, et al., Strongly luminescent Dion–Jacobson tin bromide perovskite microcrystals induced by molecular proton donors chloroform and dichloromethane, *Adv. Funct. Mater.* 31 (28) (2021) 2102182.

[26] G.W. Sun, X.Y. Liu, Z. Liu, et al., Emission wavelength tuning via competing lattice expansion and octahedral tilting for efficient red perovskite light-emitting diodes, *Adv. Funct. Mater.* 31 (50) (2021) 2106691.

[27] J.-T. Lin, C.-C. Liao, C.-S. Hsu, et al., Harnessing dielectric confinement on tin perovskites to achieve emission quantum yield up to 21%, *J. Am. Chem. Soc.* 141 (26) (2019) 10324–10330.

[28] L. Martínez-Sarti, S.H. Jo, Y.-H. Kim, et al., Low-dimensional iodide perovskite nanocrystals enable efficient red emissi032310on, *Nanoscale* 11 (27) (2019) 12793–12797.

[29] M. Mittal, A. Jana, S. Sarkar, et al., Size of the organic cation tunes the band gap of colloidal organolead bromide perovskite nanocrystals, *J. Phys. Chem. Lett.* 7 (16) (2016) 3270–3277.

[30] S. Ma, Y.K. Jung, J. Ahn, et al., Elucidating the origin of chiroptical activity in chiral 2d perovskites through nano-confined growth, *Nat. Commun.* 13 (1) (2022) 3259.

[31] J. Möbs, P. Klement, G. Stuhrmann, et al., Enhanced circular dichroism and polarized emission in an achiral, low band gap bismuth iodide perovskite derivative, *J. Am. Chem. Soc.* 145 (43) (2023) 23478–23487.

[32] A.A. Koegel, E.M. Mozur, I.W.H. Oswald, et al., Correlating broadband photoluminescence with structural dynamics in layered hybrid halide perovskites, *J. Am. Chem. Soc.* 144 (3) (2022) 1313–1322.

[33] Y.H. Kim, Y.X. Zhai, E.A. Gaulding, et al., Strategies to achieve high circularly polarized luminescence from colloidal organic-inorganic hybrid perovskite nanocrystals, *ACS Nano* 14 (7) (2020) 8816–8825.

[34] J.W. Wei, Q.L. Luo, S.G. Liang, et al., Metal halide perovskite nanocrystals for near-infrared circularly polarized luminescence with high photoluminescence quantum yield via chiral ligand exchange, *J. Phys. Chem. Lett.* 14 (24) (2023) 5489–5496.

[35] R. Lu, Z. Wen, M. Zhao, et al., Spacer cation alloying enables markedly improved chiroptical properties of two-dimensional chiral hybrid perovskite nanosheets, *Adv. Opt. Mater.* 11 (4) (2023) 2202290.

[36] H. Song, M. Kwak, W. Choi, et al., Enhancing circular dichroism in chiral perovskites via dual spacer cation engineering for circularly polarized light detection, *Adv. Opt. Mater.* 12 (31) (2024) 2401427.

[37] S. Jiang, N.A. Kotov, Circular polarized light emission in chiral inorganic nanomaterials, *Adv. Mater.* 35 (34) (2023) 2108431.

[38] D. Zhong, B. Teng, W. Kong, et al., Growth, structural, spectral, and high-power continuous-wave laser operation of Yb 0.11 Gd 0.89 Cob crystal, *J. Rare Earths* 35 (7) (2017) 637–644.

[39] K. Robinson, G.V. Gibbs, P.H. Ribbe, Quadratic elongation: a quantitative measure of distortion in coordination polyhedra, *Science* 172 (3983) (1971) 567–570.

[40] Z. Bian, J.L. Miao, Y.D. Zhao, et al., Strong interlayer interaction for engineering two-dimensional materials, *Acc. Mater. Res.* 3 (12) (2022) 1220–1231.

[41] W.B. Li, S. Sidhik, B. Traore, et al., Light-activated interlayer contraction in two-dimensional perovskites for high-efficiency solar cells, *Nat. Nanotechnol.* 17 (1) (2022) 45-+.

[42] D.B. Straus, S.H. Parra, N. Iotov, et al., Tailoring hot exciton dynamics in 2D hybrid perovskites through cation modification, *ACS Nano* 14 (3) (2020) 3621–3629.

[43] J.N. Duan, J.R. Li, G. Divitini, et al., 2D hybrid perovskites: from static and dynamic structures to potential applications, *Adv. Mater.* 36 (30) (2024) 2403455.

[44] Y. Han, J. Yin, G.Y. Cao, et al., Exciton self-trapping for white emission in 100-oriented two-dimensional perovskites via halogen substitution, *ACS Energy Lett.* 7 (1) (2022) 453–460.

[45] R. Zhou, L.Z. Sui, X.B. Liu, et al., Multiphoton excited singlet/triplet mixed self-trapped exciton emission, *Nat. Commun.* 14 (1) (2023) 1310.

[46] M. Mączka, D. Drozdowski, D. Stefańska, et al., Zero-dimensional mixed-cation hybrid lead halides with broadband emissions, *Inorg. Chem. Front.* 10 (24) (2023) 7222–7230.

[47] X.B. Han, C.Q. Jing, H.Y. Zu, et al., Structural descriptors to correlate Pb ion displacement and broadband emission in 2d halide perovskites, *J. Am. Chem. Soc.* 144 (40) (2022) 18595–18606.

[48] F.F. Gao, Y. Qin, Z.G. Li, et al., Unusual Pressure-induced self-trapped exciton to free exciton transfer in chiral 2D lead bromide perovskites, *ACS Nano* 18 (4) (2024) 3251–3259.

[49] L. Zhou, J.-F. Liao, Z.-G. Huang, et al., Intrinsic self-trapped emission in 0d lead-free $(C_4H_{14}N_2)_2In_2Br_{10}$ single crystal, *Angew. Chem. Int. Ed.* 58 (43) (2019) 15435–15440.

[50] R. Laref, F. Massuyeau, R. Gautier, Role of hydrogen bonding on the design of new hybrid perovskites unraveled by machine learning, *Small* 20 (5) (2023) 2306481.

[51] Y.J. Niu, D.C. He, Z.G. Zhang, et al., Improved crystallinity and self-healing effects in perovskite solar cells via functional incorporation of polyvinylpyrrolidone, *J. Energy Chem.* 68 (2022) 12–18.

[52] Y. Du, J. Wu, X. Zhang, et al., Surface passivation using pyridinium iodide for highly efficient planar perovskite solar cells, *J. Energy Chem.* 52 (2021) 84–91.

[53] Z.-G. Yu, Chirality-induced spin-orbit coupling, spin transport, and natural optical activity in hybrid organic-inorganic perovskites, *J. Phys. Chem. Lett.* 11 (20) (2020) 8638–8646.

[54] M.P. Davydova, L. Meng, M.I. Rakhmanova, et al., Strong magnetically-responsive circularly polarized phosphorescence and X-ray scintillation in ultrarobust Mn(Ii)–organic helical chains, Adv. Mater. 35 (35) (2023) 2303611.

[55] C. He, J. Qiu, Z. Mu, et al., Room temperature circularly polarized emission in perovskite nanocrystals through bichiral-molecule-induced lattice reconstruction, *Matter* 7 (2) (2024) 475–484.

[56] C.L. He, Z.Y. Feng, S.Z. Shan, et al., Highly enantioselective photo-polymerization enhanced by chiral nanoparticles and in situ photopatterning of chirality, *Nat. Commun.* 11 (1) (2020) 1188.